Materials & Design 233 (2023) 112224

Contents lists available at ScienceDirect

Materials & Design

journal homepage: www.elsevier.com/locate/matdes

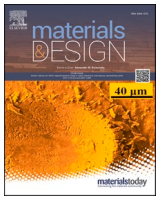

On sustainable design and manufacturing for the footwear industry – Towards circular manufacturing

Chahine Ghimouz, Jean Pierre Kenné, Lucas A. Hof *

Mechanical Engineering Department, École de technologie supérieure, 1100, rue Notre-Dame Ouest, Montreal, Québec H3C1K3, Canada

ARTICLE INFO

Keywords:
Circular manufacturing
Additive manufacturing
Selective laser sintering
Snapfit design
Topology optimisation
Linear elasticity modeling

ABSTRACT

The global fashion industry is facing carbon footprint issues, but technological innovations are helping to improve its performance and environmental efficiency in terms of footwear manufacturing. This paper explores how Design for Additive Manufacturing (DfAM), Design for Assembly (DfA), and Design for Disassembly (DfD) strategies, along with Additive Manufacturing's (AM) capability to produce intricate parts, can contribute to the fashion industry's shift towards a Circular Manufacturing model. The focus is on footwear manufacturing and its carbon footprint issues. The proposed additively manufactured shoe design utilizes Polyamide 12 and Thermoplastic polyurethane as feedstock, featuring a glueless mechanical assembly system based on a snapfit. Notably, the upper part of the shoe incorporates a variable lattice structure to ensure flexibility in different areas. Finite Element Analysis (FEA) demonstrates that the snapfit assembly exceeds the industry standard's minimum disassembly force requirement. Additionally, an optimization algorithm for the variable lattice structure results in a 34% mass reduction while maintaining the desired Young's modulus in each shoe zone. This design approach aligns with the footwear industry's sustainability goals, aiming to reduce environmental impact and enhance product durability. The study successfully developed a strategy to implement AM for sustainable shoe fabrication.

1. Introduction

The global consumption of natural resources is constantly increasing in this 21st century. Nowadays, the quantities of annually consumed natural resources worldwide are so excessive that their consumption occurs at a higher rate than required for their regeneration by the planet [1]. In fact, it currently takes the planet earth 1.7 years to regenerate all the resources consumed in one year [2]. In 2010, 72 billion tons of raw materials were extracted and consumed, twice the amount extracted in 1980, according to a 2015 report by the Organization for Economic Cooperation and Development [3]. With the current economical growth, annual consumption will reach the symbolic 100-billion-ton mark around 2030 [4]. However, the corresponding human activity is progressively emitting anthropogenic greenhouse gases (GHG) each year, exceeding 48.9 giga tons of CO_2 equivalent (CO_2-eq) in 2018 as reported by Climate Watch Data [5]. From these annual GHG emissions, an amount of 1.7 giga tons of CO_2-eq were emitted only by the textile and footwear industry in 2015 and if this trend continues, the BCG Retail value project predicts 2.7 giga tons of CO_2-eq emitted by this industry in 2030 [6], representing an increase of 63%. As well, the waste generation from the clothing and footwear industry will increase from 92 mega tons in 2015 to 148 mega tons in 2030 [6]. In addition, only 5% of footwear is recycled globally [7], which results in sustainability issues for this industry.

This acceleration of raw material consumption and GHG emissions in the manufacturing industry is partly due to the actual typical linear economic model (*Take*, *Make*, *Use* and *Throw*), also referred to as the "linear economy" (LE) [8]. To address this issue of overconsumption and the environmental challenge that the planet is experiencing [9], a more sustainable model has been proposed; the "circular economy" (CE). This approach, derived from initiatives dating back to the 1970 s [10], presents the economy as a business mindset that will enable a shift towards long-term sustainable development [11] including a principle concept based on the 6Rs (*Reuse, Recycle, Redesign, Remanufacture, Reduce, and Recover*) [12]. Based on these developments, the "circular manufacturing" (CM) model is emerging as one of the engineering solutions to consider for sustainable production [13]. In such a CM model, the product design, used materials, and its manufacture play an essential

* Corresponding author.
E-mail addresses: chahine.ghimouz.1@ens.etsmtl.ca (C. Ghimouz), Jean-Pierre.Kenne@etsmtl.ca (J.P. Kenné), lucas.hof@etsmtl.ca (L.A. Hof).

https://doi.org/10.1016/j.matdes.2023.112224
Received 26 May 2023; Received in revised form 1 August 2023; Accepted 3 August 2023
Available online 5 August 2023

role in the product's recyclability [14]. More specifically, a "circular design" process includes rethinking the product design not only for its end-use, but also for its user environment and process steps at its end-of-life (EOL) state to favor reuse, facilitating its reinsertion in a closed manufacturing loop and ultimately disassembly for improved recyclability [15].

In such circular manufacturing systems, design for assembly (DfA) and design for disassembly (DfD) strategies are key methodological elements for product and process development aimed at reducing costs and improving reliability without changing product function [16]. These DfA and DfD approaches are based on some specific design principles including: *Reduce the number of parts*; *Simplify the design*; *Design for easy assembly and disassembly*; *Design for efficient joining and fastening*; *Minimize flexible parts and interconnections*; *Standardize parts and materials*; and *Design modular products*.

Additive manufacturing (AM), or 3D printing, which is a relatively new technology [17], has an interesting potential for circular manufacturing, by reducing waste, energy consumption and manufacturing costs at small production scales [18]. It also facilitates reuse by creating parts in modular designs that facilitates their reuse and repair [19]. In addition, AM enables the development of sustainable products by considering sustainable and circular development principles from the beginning of the design process. This can result in products that are more sustainable and easily recyclable or reusable at the end of their life [19,20].

In 2019, a record-year regarding the volume of produced footwear, 24.3 billion pairs were produced and sold or more than 65 million pairs of shoes per day [21]. However, footwear manufacturing is a labor-intensive process, as typical footwear products consist of 65 individual parts including around 360, mostly manual, manufacturing steps [22]. This traditional manufacturing approach is still highly labor and machine intensive for footwear part production and final product assembly. Consequently, footwear manufacturers are looking for new ways to optimize their manufacturing process [23]. AM offers a promising alternative allowing footwear manufacturers to streamline the production of certain shoe components [24–26].

However, these developments are still in their infancy, and it is difficult to produce fully 3D printed footwear due to the high rejection rate caused by manufacturing defects [27]. To date, 3D printing is primarily only used to manufacture specific footwear parts, such as the midsole, which is the shock-absorbing layer between the insole and the outsole. The mechanical performances of the used materials are different from one to another and have very distinct applications. However, the steps involved in the AM process are critical to increase the capabilities of functional prototypes. Hence, a good understanding of key process parameters, such as build orientation, print speed, and layer thickness, affect mechanical properties [28], and research is just emerging in this field [29].

1.1. Additive manufacturing

Compared to conventional polymer manufacturing processes, such as injection moulding, thermoforming, or extrusion [30], additive manufacturing (AM), or 3D printing, is a relatively new manufacturing process, debuting from the 1980 s, that has not yet reached its full maturity [31]. Among the seven AM technologies defined in the ISO/ASTM 52900:21 standard [32], powder bed fusion (PBF) of polyamide 12 (Nylon 12 or PA12) is considered as the most mature technology for industrial product applications [33]. The most widely used AM technologies for PBF are Multi Jet Fusion (MJF) [34] and Selective Laser Sintering (SLS) [34]. SLS uses a laser to melt and fuse the feedstock powder, while MJF uses a bonding agent, heat and infrared light to fuse the powder to create the final object. Both technologies involve heating of feedstock powder particles, with typical size between 45 and 90 μm [35], to sinter and consolidate the particles layer by layer to form a three-dimensional (3D) object. Compared to conventional manufacturing, AM provides high geometric freedom in design and fabrication [36]. In addition, PBF AM processes facilitate product manufacturing for mass customization, weight reduction, surface texturing and dimensional accuracy [37], which opens up new manufacturing opportunities for biomimicry based designs, e.g. by replicating natural cellular materials to achieve heterogenic mechanical behaviour of monolithic material. Reducing the number of different types of material is interesting for circular design and manufacturing strategies, as it facilities the product disassembly and recycling processes at a product's EOL [38,39].

To date, polymer AM is emerging for functional applications in different domains, such as the medical industry [40], the automotive industry [36], the aerospace industry, and as spare parts for maintenance [41]. Nevertheless, a remaining challenge of these layer-based manufacturing methods is the generation of anisotropic mechanical properties, i.e. the parts' properties are directly dependent on its orientation during printing and the layer thickness [42]. In addition to low manufacturing speeds, post-processing is also required to ensure a satisfying surface finish for functional parts in industrial applications [43]. However, the anisotropic nature of the properties can be exploited for specific applications by studying this property in depth and controlling factors influencing it. The creation of architectured material is an excellent way to achieve this.

1.2. Architectured materials

Natural cellular materials such as wood, cork or bone have been well used for centuries, and their structure is imitated in modern engineering materials such as honeycombs and foams to take advantage of their specific mechanical properties due to their porosity. This bio-inspired engineering field opens up many new possibilities, resulting in the creation of architectured materials such as lattice structures [44]. AM and more specifically SLS is very well suited for the fabrication of such structures, hence the relatively large number of studies on this topic [45]. Lattice structures are three-dimensional periodic arrangements of a unit cell resulting in a coherent and homogeneous material with specific mechanical and thermal properties. The type of unit cell can be divided into three main classes, which are 1) *strut-based lattices*, 2) *planar lattices*, and 3) *surface-based lattices*, where each category demonstrates different mechanical behavior [44].

The control of the lattice structures' mechanical properties depends strongly on its class as well as on its type, such as diamond, gyroid or other [46]. Recent literature revealed that depending on the nature of the macroscopic loading, the structure deforms with a combination of bending, torsion or stretching of the lattice struts [47]. The mechanical properties' dependence on the structure's density is impacted by the loading mode it is exposed to [48]. In fact, the sheet type *Triply Periodic Minimal Surface (TPMS)*, belonging to the *surface-based lattices* class, depends the least on its relative density and it has the highest modulus of elasticity and mechanical strength for the same density compared to the other classes [46]. Hence, this sheet TPMS surface-based lattice type provides a large design space to control the mechanical properties of the architected material. Therefore, this lattice type and class have been chosen for the present study.

Current architecture materials applications are mainly in the biomedical and aerospace field. The main use of lattice structures in the biomedical field is focused on implant designs to control their mechanical properties (e.g. Young's modulus) in order to approach bone behavior and optimal osseointegration capability. The aerospace industry appreciates the high thermal capabilities of lattice structures and the potential to reduction the number of parts while keeping a similar mechanical strength. Nevertheless, one of the limitations of cellular structures is their behavior under cyclic loading; the fatigue behavior is directly related to the density of the material and, therefore, fractures occur in fewer cycles for lattice structures compared to bulk materials [44].

1.3. Objectives and contributions of the present study

The main objective of this study is to develop a CM approach for footwear manufacturing using AM techniques to increase their remanufacturability and recyclability by focusing on a design for disassembly. The novelty of the presented approach includes the development of an entirely AM-based footwear manufacturing process to achieve footwear (high heels) that are easy to disassemble and offer an adaptable design approach to optimize user comfort by topological optimization. AM offers new design possibilities that are exploited in the developed production strategy to reduce the number of footwear parts and to achieve glue-less component assembly, which favors disassembly for remanufacturing and recycling when reaching the end-of-life stage of the shoes.

This paper is organized as illustrated in Fig. 1 and started by introducing the background and current state-of-the-art of AM and its use as production method for polymer parts in section 1. Section 2.1 presents the used materials, and design methodology, e.g. for the assembly system and the topological optimization, followed by the presentation of the developed footwear prototype including both analytical and numerical finite element analysis (FEA) validations for critical shoe elements, such as the heel and outsole (section 2.2) and a discussion on the design workflow for the high-heel upper part development (section 2.3). The obtained results are presented and discussed in section 3. Finally, the conclusions of the developed work on CM for footwear and an outlook towards future studies are outlined in section 4.

2. Materials, design and methods

The overarching methodology of the present study includes: 1) design of a 3D printable footwear prototype (high-heel), 2) material and AM technology selection and characterization, 3) design of a glue-less mechanical assembly system, and finally 4) topological optimization and weight reduction to improve footwear user's comfort and to reduce the quantity of used material. Section 2.1 discusses the developed high-heel prototype, which was designed using a Design for Additive Manufacturing (DfAM) approach [49]. Fusion 360 [50] and CATIA V5 3D modeling software [51] were adopted in this design step. Section 2.2 details the selected materials and its mechanical characteristics, as well as the sample preparation by the selected AM technology and post-processing method to validate and compare the material's properties net-printed and post-treated. Section 2.3 outlines the glue-less assembly system for the different printed footwear parts and its adopted DfA [52] and DfD [52] strategies based on snap-fit part connections. A concept for the high-heel reinforcement integration is analysed and presented as well. Section 2.4 discusses the topological optimization for the selected sheet type TPMS surface-based lattice structure, which was performed using the *nTop platform* and *nTopcl* from the nTopology software [53].

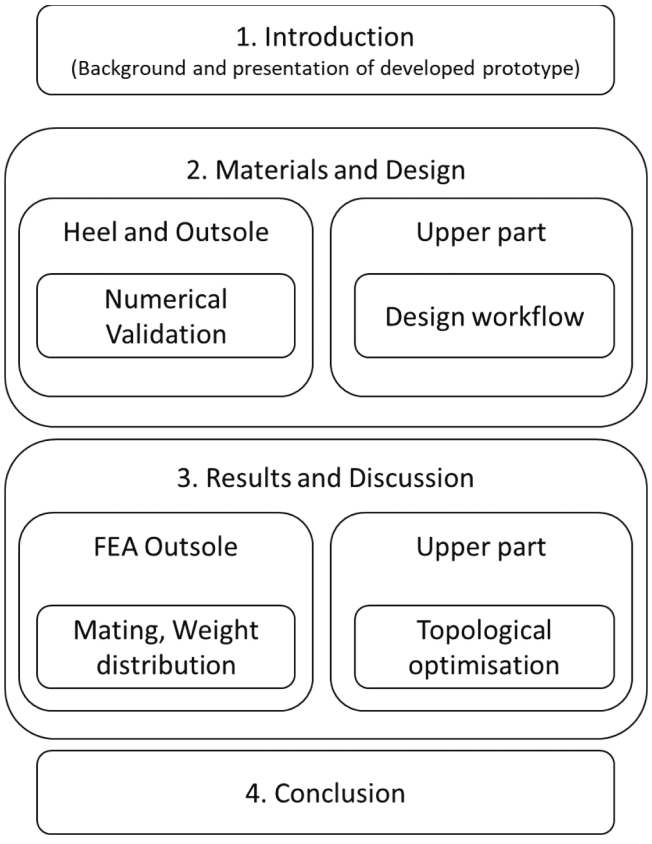

Fig. 1. Schematic illustration representing the structure of the present study.

Fig. 2 illustrates the different steps of the adopted methodology to achieve sustainable and additive manufacturing of footwear (here: a high-heel). In a first step, typical AM suitable polymeric material is selected and characterized on mechanical performance. Secondly, a footwear prototype model is proposed including the simulation of the load distribution (foot) during usage. In a third step, the assembly system to integrate the individual footwear components into a product (high-heel) is developed including numerical simulations for functional and strength validation. Finally, a topological optimization of the developed high-heel has been performed to determine the most appropriate lattice structure for upper part of the final footwear product. Details and preliminary design results for each step are presented in section 2.1, 2.2, 2.3, and 2.4 respectively.

2.1. Prototype design

A high-heeled shoe is traditionally composed of more than 60 pieces per pair. However, new production possibilities are appearing with the arrival of new manufacturing technologies, notably 3D printing. This enables the design of more complex parts and the capacity to merge different footwear assemblies into one monolithic part, thereby reducing the risks of defects due to the assembly, as well as accommodating shoe disassembly followed by repurposing (remanufacturing or recycling) at its EOL state.

The prototype design considered to the integration of key footwear parts to maintain three (3) functional parts that will be used in the assembly; the *outsole*, *insole* and *upper part* as shown in Fig. 3 The outsole will be subjected to the load distribution applied to the shoe due to a user's weight and therefore it must be able to withstand this load with a specified safety factor. The insole must have a certain amount of flexibility (low stiffness) to ensure the users' comfort when wearing the shoe. Similarly, the upper part - being in direct contact with the skin and having the role of containing the foot – needs to have a specific stiffness to ensure the comfort of the shoe while keeping a certain resistance to tearing.

2.2. Printing material and technology

Based on their mechanical properties (see Table 1), two materials were selected in the developed novel footwear concept: polyamide 12 (also called nylon 12 or PA12) and a thermoplastic polyurethane (TPU). The nylon 12 material *PA2200* from EOS [54] was selected for the *outsole* and the thermoplastic polyurethane LUVOSINT TPU X92A-1 NT from LEHVOSS Group [55] for the *upper part* and the *insole*.

Both materials were used for the fabrication of ASTM D638-14 [56] standardized tensile test samples by selective laser sintering (SLS) (see Fig. 4). The EOS FORMIGA P110 Velocis machine and the FARSOON 252P HT machine were used as SLS machines for the PA12 and TPU based materials, respectively.

The orientation of the SLS printing was done in the lateral XY plane as shown in Fig. 4 and 100% virgin powder was used as feedstock. In

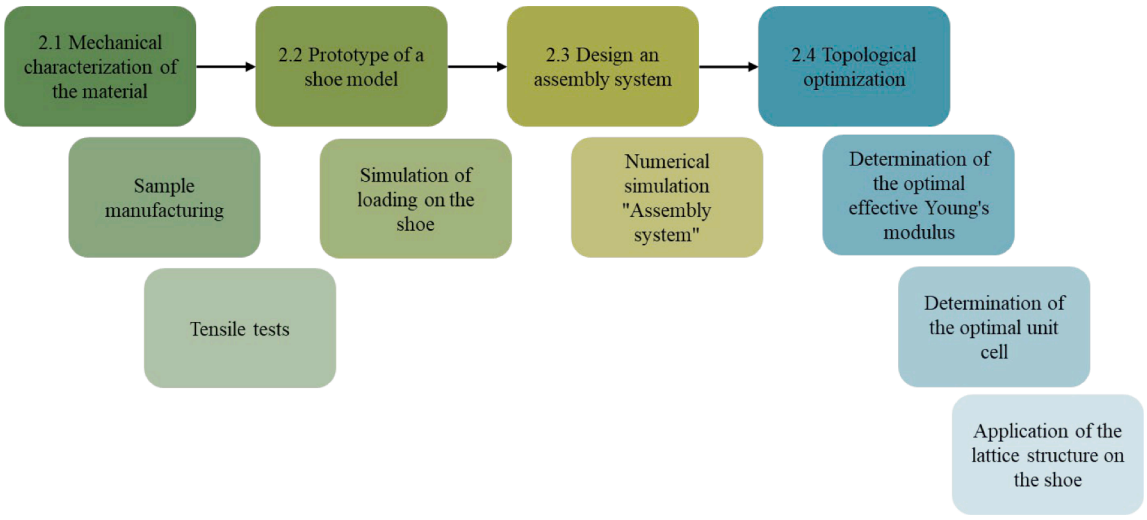

Fig. 2. The adopted methodology to achieve this study's objectives on sustainable footwear development.

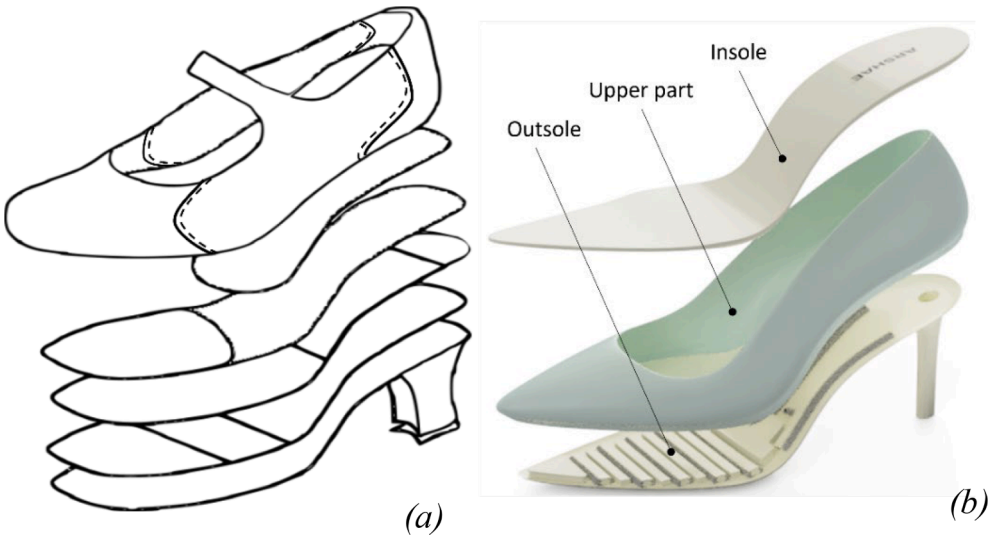

Fig. 3. Illustration of the assembled high-heeled shoe after reduction of the number of parts, (a) simplified traditional shoe, (b) developed prototype.

Table 1
Mechanical properties provided by the manufacturer.

Materials	Tensile Strength (MPa)	Young modulus (MPa)	Elongation at break (%)
PA2200	48	1650	18
LUVOSINT TPU X92A-1 NT	20	92*	520

* Shore hardness A.

order to assess the influence of postprocessing on the SLS printed samples' mechanical properties (e.g. Young's modulus, Tensile Strength, Elongation at break), half of the printed polyamide specimen batch (lot size: $n = 16$) did undergo a chemical surface treatment by Vapor Polishing [57] on a POSTPRO SF100 machine (AMTechnologies) and the other half of the batch was left untreated.

Hence, to compare the mechanical properties of the PA2200 material as printed and vapor polished, for further use in this work, tensile tests were performed with a 10kN load cell on an MTS Alliance RF/200 machine at 23 °C and 50% humidity.

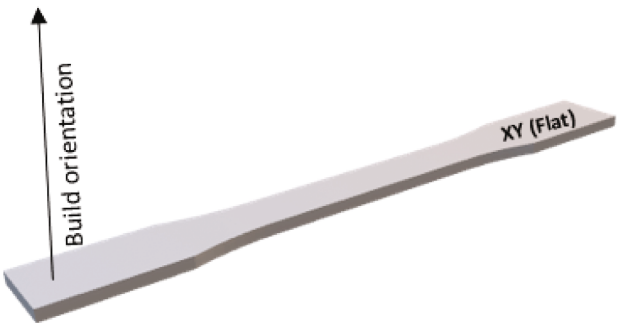

Fig. 4. Specimen orientation during printing.

2.3. Design of the mechanical assembly system

To achieve footwear disassembly for complete repurposing (remanufacturing or recycling) at its end-of-life, it is essential to eliminate the use of chemical glue during the shoe assembly process. Avoiding the use of glue facilitates footwear parts disassembly for their individual recycling. Therefore, in this study, we have developed an exclusively

mechanical assembly system instead of using chemical connections. The proposed assembly system has been divided into two parts, the first part consists of designing an assembly system for the front part of the shoe, which is beyond the scope of this work, the second part consists of developing a mechanical system for the rear part of the shoe (at the heel). A snapfit system is proposed to assemble the upper and the outsole as shown in Fig. 5. An aluminum pin (cross-section shown in yellow in Fig. 5(a), and a 3D image presented in Fig. 5(b)) has been inserted into the heel to increase the lateral impact resistance.

The snap-fit connection was designed according to the guidelines proposed by Bonenberger [58]. Analytical calculations of snap-fit parameters, such as assembly and disassembly forces and maximum rod deflections, were performed to dimension and validate the preliminary design.

The equations used in this section are based on the work of Ticona [59] on snap-fit connections of plastic parts. The maximum deflection of each rod in the snap connection is calculated as follows by Eq. (1):

$$H_{max} = 0.555 \frac{l^2}{r} \frac{\varepsilon_{max}}{100} \tag{1}$$

Where H_{max} is the maximum deflection in mm, l is the length of the snapfit legs in mm, r is the outer radius of the circular legs in mm, and ε_{max} is the maximum allowable strain (recommended to be 1/3 of the ultimate strain [59]).

Using a snapfit legs' length (see Fig. 5.(c)) of 3.5 mm and a outer radius of 2 mm in Eq.1 results in a maximum deflection H_{max} of 5.9 mm to reach the allowable limits with a strain of 1/3 of 520% according to our design (maximum elongation provided by the manufacturer of the selected TPU X92A-1 NT) [55].

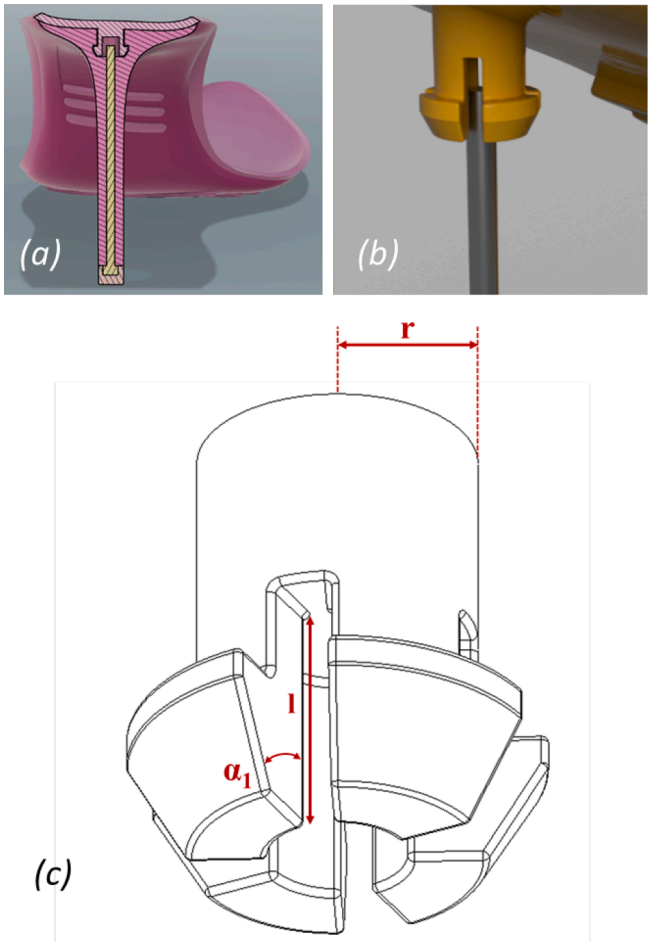

Fig. 5. Cross section **(a)** illustrating the integration of the snapfit in the shoe, **(b)** integration of the male part of the snapfit to the upper part, and **(c)** illustration of the developed snapfit dimensional parameters.

To calculate the joining force, $F1$, the following equations (2) and (3) were deployed:

$$F1 = \frac{3HE_sJ}{l^3} \frac{\mu + \tan\alpha 1}{1 - \mu\tan\alpha 1} \tag{2}$$

$$J = 0.0508r^4 \tag{3}$$

Note that H is the bending of the snapfit legs (designed as $H = 2.5$ mm for proper mating), E_s is the secant modulus of elasticity calculated from the data obtained by performing tensile tests according to ASTM D638 on the selected LUVOSINT TPU X92A-1 NT material (resulting in $Es = 37$ MPa), J is the moment of inertia based on the study of Ticona [59], l is the length of the legs, μ is the coefficient of friction, and $\alpha 1$ is the assembly angle of the legs (here $\alpha 1 = 30°$). The coefficient of friction was estimated to be $\mu = 0.329$ after consulting the work on "Surface quality improvement of selective laser sintered polyamide 12" by Guo, Bai, Liu, and Wei [60] and the previously cited design guide [58], which prescribes a coefficient of friction μ between 0.3 and 0.4 for polyamide 12 material.

Equations (1), (2) and (3) give us a force per rod equal to 5.9 N which must be multiplied by the number of snapfit legs, which is 4 in our case, giving us the mounting force of 23.6 N.

The disassembly force, $F2$, for a 90° angle can be calculated with the equation (4)

$$F2 = A\tau_b \tag{4}$$

With A being the shear area (Fig. 6) of the rod and τ_b being 60% of the ultimate stress of the material used (0.6 × 20 MPa). This results in a disassembly force of $F2 = 156$ N per rod, which we multiply by 4 to obtain the total force, or 624 N (63.63 kgf) for the TPU X92A-1 NT material, which is significantly higher than the normal force resistance applied for high heel pull-off as recommended by the SATRA TM113:1996 footwear standard (40kgf).

2.4. Topology optimisation and weight reduction

Additive manufacturing is emerging in the fashion sector, and especially the footwear industry. Specific interest has been reported on the exploitation of the full design potential provided by AM technology, i.e. the creation of parts with complex geometries, for example

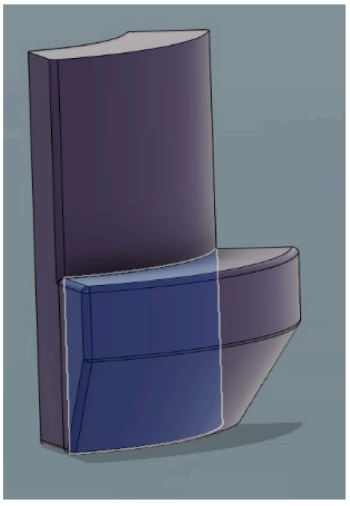

Fig. 6. Illustration of a quarter of the designed circular snapfit legs, including the surface A (highlighted in blue) that is used in equation (4) to calculate the disassembly force. (For interpretation of the references to colour in this figure legend, the reader is referred to the web version of this article.)

witnessed by the use of lattice structures for shoe soles [61]. There is abundant literature on this subject, which focuses mainly on the sole design to improve users' comfort [62,63] by absorbing the energy transmitted to the sole during walking or running.

The present study proposes to address the comfort issue for the one-piece printed high-heel shoe by topological optimization of the monolithic material based upper part to approach the comfort offered by conventionally manufactured heterogenic material-based footwear. It should be noted, that in the current footwear market the approach chosen by manufacturers is to use different materials with different density and mechanical properties to optimize the absorption of energy due to walking.

Fig. 7 illustrates the Shore A hardness gradient for high-heeled shoes as recommended by industrial shoe designers. A conversion of the Shore A hardness is therefore necessary towards a mechanical property that can be manipulated by architectural materials. This study proposes to use the Young's modulus which has several methods of conversion to Shore A hardness [64–66].

Table 2 presents the conversion results according to different developed Shore A hardness – Young's modulus conversion methods, i.e. the Gent Function, the Error Function, the Ruess Function, and Mix & Giacomin's method. The conversion relations for each method are presented below by equations (5), (6), (7) and (8) from literature studies, respectively [64–66].

$$[\text{Gent Function}]\mathrm{Y} = (0.0981(56 + 7.62336\,\mathrm{S_A}))/(0.137505(254 - 2.54\,\mathrm{S_A})) \tag{5}$$

$$[\text{Error Function}]\mathrm{S_A} = 100\mathrm{erf}\,(3.186\,10^{-4}\sqrt{\mathrm{Y}}) \tag{6}$$

$$[\text{Ruess Function}]\mathrm{Y} = 10^{0.0235\,\mathrm{S_A} - 0.6403} \tag{7}$$

$$[\text{Mix \& Giacomin}]Y = (3F_0(1 + MiS_A)/(1 - S_A))/8p_0r \tag{8}$$

In these relations Y represents the Young's modulus and S_A the value indicated by the durometer according to ASTM D2240-05 [67]. In equation (8), Mi is the mechanical indentability, which can be calculated using equation (9) [66]

$$Mi = kp_0/\sigma F_0 \tag{9}$$

where k is the stiffness constant of the spring mounted inside the durometer, and the constants F_0, p_0 and r equal the values of 0.55 N, 0.25 cm, and 0.0395 cm respectively [66]. These constants are the characteristics of the durometer used for the Shore A scale [66].

Since not all the methods presented above give the same result, the method of Mix and Giacomin [66] was chosen for this study as their method is suggested by the ASTM standard D2240-15(2021) [66,67], as typically adopted by industry.

To create an appropriate lattice structure for the upper part of the shoe, an optimization algorithm was developed using Python and the nTop platform via nTopcl (nTopology Inc [53]), as a tool for creating lattice structures. The design was based on the TPMS type, which is considered as the most appropriate lattice type for small thickness structures. The material properties were determined using the numerical homogenization method [68,69], which involved applying boundary conditions [70,71] on a finite element model representing a unit cell in a periodic structure. The homogenized elastic properties of the material are calculated from the displacement fields associated with six-unit strain loads in the X, Y, Z, XY, YZ, ZX directions under periodic boundary conditions. The nTop platform allows to test the elastic response of each created unit cell and it enables to determine the stiffness tensor of the structure according to the different directions in the form of a 6x6 sized matrix, using the generalized Hooke's law $\sigma_{ij} = C_{ijkl}\varepsilon_{kl}$, where σ_{ij}, ε_{kl}, and C_{ijkl} are the components of the Stress, strain and stiffness tensor respectively, which we can be represented as follows (Eq. (10)) using Voigt's notation:

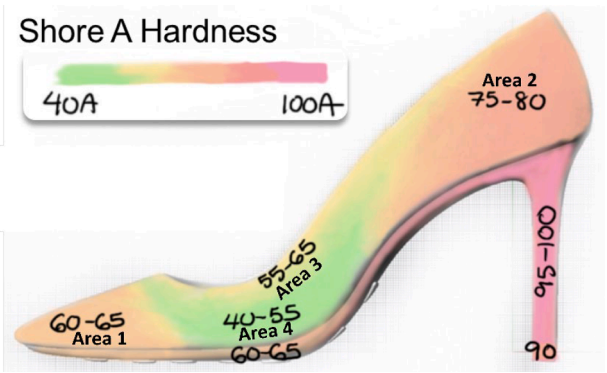

Fig. 7. Illustration of the Shore A hardness in different areas of the shoe.

Table 2
Conversion of Shore A hardness to Young's modulus using different methods.

Areas	Shore A	Gent function (MPa)	Reuss function (MPa)	Error function (MPa)	Mix and Giacomin Method (MPa)
1	60–65	3,6–4,42	5,88–7,71	3,48–4,3	4,79–5,88
2	75–80	7,05–9,35	13,24–17,36	6,5–8,09	9,38–12,43
3	55–65	2,96–4,42	4,48–7,71	2,81–4,3	3,94–5,88
4	40–55	1,68–2,98	1,99–4,48	1,35–2,81	2,24–3,94

$$\begin{pmatrix}\sigma_1\\ \sigma_2\\ \sigma_3\\ \sigma_4\\ \sigma_5\\ \sigma_6\end{pmatrix} = \begin{bmatrix} c_{11} & c_{12} & c_{13} & c_{14} & c_{15} & c_{16}\\ c_{21} & c_{22} & c_{23} & c_{24} & c_{25} & c_{26}\\ c_{31} & c_{32} & c_{33} & c_{34} & c_{35} & c_{36}\\ c_{41} & c_{42} & c_{43} & c_{44} & c_{45} & c_{46}\\ c_{51} & c_{52} & c_{53} & c_{54} & c_{55} & c_{56}\\ c_{61} & c_{62} & c_{63} & c_{64} & c_{65} & c_{66}\end{bmatrix} \begin{pmatrix}\varepsilon_1\\ \varepsilon_2\\ \varepsilon_3\\ \varepsilon_4\\ \varepsilon_5\\ \varepsilon_6\end{pmatrix} \tag{10}$$

In the case of cubic elasticity, the stress is written as shown in equation (11). Then, the following relations for the stiffness tensor components are deployed: $C_{11} = C_{22} = C_{33}, C_{12} = C_{21} = C_{13} = C_{31} = C_{23} = C_{32}, C_{44} = C_{55} = C_{66}$, and the rest of the components are equal to zero:

$$\begin{pmatrix}\sigma_1\\ \sigma_2\\ \sigma_3\\ \sigma_4\\ \sigma_5\\ \sigma_6\end{pmatrix} = \begin{bmatrix} c_{11} & c_{12} & c_{12} & 0 & 0 & 0\\ c_{12} & c_{11} & c_{12} & 0 & 0 & 0\\ c_{12} & c_{12} & c_{11} & 0 & 0 & 0\\ 0 & 0 & 0 & c_{44} & 0 & 0\\ 0 & 0 & 0 & 0 & c_{44} & 0\\ 0 & 0 & 0 & 0 & 0 & c_{44}\end{bmatrix} \begin{pmatrix}\varepsilon_1\\ \varepsilon_2\\ \varepsilon_3\\ \varepsilon_4\\ \varepsilon_5\\ \varepsilon_6\end{pmatrix} \tag{11}$$

To obtain the shear coefficient G and the Poisson ratio ν from the compliance tensor S, it is necessary to invert the stiffness tensor using $\varepsilon = C^{-1}\sigma$ and $C^{-1} = S$. The compliance tensor can then be presented by:

$$S = \begin{bmatrix} 1/Y & -\nu/Y & -\nu/Y & 0 & 0 & 0\\ -\nu/Y & 1/Y & -\nu/Y & 0 & 0 & 0\\ -\nu/Y & -\nu/Y & 1/Y & 0 & 0 & 0\\ 0 & 0 & 0 & 1/G & 0 & 0\\ 0 & 0 & 0 & 0 & 1/G & 0\\ 0 & 0 & 0 & 0 & 0 & 1/G\end{bmatrix} \tag{12}$$

with

$$G = \frac{Y}{2(1+\nu)} \tag{13}$$

Here, Y is the Young's modulus, ν is the Poisson's ratio and G is one of the shear coefficients. The full mathematical homogenization model,

that was used in this study, will not be developed here, since it is not the focus of this work. More details on this adopted model can be found in literature [70,71].

The chosen independent variables are the type of unit cell, the thickness of the cell walls, and the dimensions of the box containing the cell as presented in Table 3. The algorithm implemented for the creation of the optimized model of the lattice structure that meets the given constraints (Young modulus) at each point of the shoe. Fig. 8 illustrates the implemented workflow to achieve this design optimization goal, which consist of two phases. The automatic phase includes an optimization program that has the coordinates of a point cloud and the associated target as input, and the output of this program consists of the values of the independent variables that allowed us to reach the targeted effective Young's module (Y*). The manual phase consists in creating a mesh of the model with the requested mesh quality (noting that the gradual transition of unit cell geometric parameters between the zones depends greatly on the size of the chosen mesh) and subsequently extracting the point cloud that corresponds to the nodes of the mesh. After the automatic phase, it is necessary to implement the results of the topological optimization to the point cloud using the "*Ramp bloc*" function on the nTop platform to ensure a gradual evolution of the dimensions of the unit cells in order to obtain a more refined and aesthetical final model and product.

3. Results and discussion

This section presents the obtained results on the development of the proposed high-heel shoe. It starts by presenting the results of the tensile tests performed on the used material (section 3.1), followed by a numerical FEA simulation of the snapfit assembly to validate the realized geometry and dimensions (section 3.2). The results of a static study on the weight distribution on the Outsole will be presented in section 3.3, and the results of the topological optimization algorithm performed on the upper part are discussed in section 3.4.

3.1. Tensile strength tests

Tensile tests were performed to determine the main mechanical characteristics of each material (modulus of elasticity, ultimate strength, and ultimate elongation) for their implementation in the numerical simulation software to validate the proposed designs. Tensile tests were performed according to the ASTM D638-14 protocol [56] at a strain rate of 50 mm/minute on 8 specimens per type at an ambient temperature of 21°± 0.5. The average results of the tensile strength tests are presented in Table 4. These results show the differences on the mechanical properties for the surface treated samples and the as-printed samples. It can be clearly observed that there is a statistically significant increase (p-value < 0.0001) in the ultimate strength (UTS) of the vapor polished samples, however the elongation at break (E) and the Young's modulus (Y) do only very slightly differ between the treated and as-printed parts. This small difference may be due to the manufacturing variability of the SLS printed specimens. As well, it should be noted that this difference in the average Y between the as-printed and vapor polished samples is 2.04%, which is within the normal variability of the PA2200 AM feedstock, which is about 5.8% for the SLS printing technology [72].

Fig. 9 presents a typical stress–strain curve of an as-printed and vapor polished Nylon 12 specimen. The higher tensile strength for vapor polished samples compared to the as-printed specimens can be clearly witnessed in this figure, as well as the similarity in Young's modulus for both samples.

3.2. Simulation of snapfit mate

The NASTRAN solver version 17.0.0.21 [73] through the Fusion 360 software [50] was used to perform a dynamic FEA to analyze occuring stresses and strains of the snapfit legs during mating of the circular snapfit. Concerning the boundary conditions, the female part (PA12) was fixed in all degrees of freedom, and a vertical movement with velocity of 4 mm/s was induced to the male part (TPU). A global coefficient of friction between all faces was set at 0.329 [60].

Fig. 10 shows a mapping of the equivalent Von Mises stress in MPa and the equivalent strain on the male part of the TPU snapfit. It can be clearly identified that the Von Mises stress reaches a maximum of 11.7 MPa and does not exceed the tensile strength of the TPU X92A-1, which is equal to 20 MPa according to the supplier. Note that a very small strain is applied for the snapfit assembly.

Fig. 11 shows the evolution of the von Mises stress as a function of time during assembly at the critical point of the snapfit (the radius at the base of the cylindrical snapfit legs). It can seen that the highest stress reached here is 6 MPa knowing that the TPU X92A-1 used for this part has a tensile strength of 20 MPa according to the data sheet provided by the manufacturer [55]. Hence, the simulation validates the design of the developed snapfit printed in TPU X92A-1.

3.3. Static study

This section will focus on a static study (no evolution of the load as a function of time) and will be divided into 3 subsections, which will cover respectively plantar division useful for mapping the load on the shoe, the weight distribution, and the stresses of the shoe with the integration of snapfit.

3.3.1. Plantar division

The sole of the feet is divided into eight (8) anatomical zones based on the work of Shang et al. [43], these zones are referred to as (T1): big toe, (T2-5): small toe, (M1): first metatarsal, (M23): central forefoot, (M45): lateral forefoot, (MF): midfoot, (MH): medial heel, (LH): lateral heel. These plantar areas are shown in Table 5.

Table 3
Description of the used independent variables.

Designation	Range
Wall thickness (mm)	[0.06 to 0.1]
Size UVW (mm) $U = V = W$	[2 to 5]
Lattice cell type (TPMS)	Gyroid, Shwarz, Diamond, Lidinoid, SplitP, Neovius

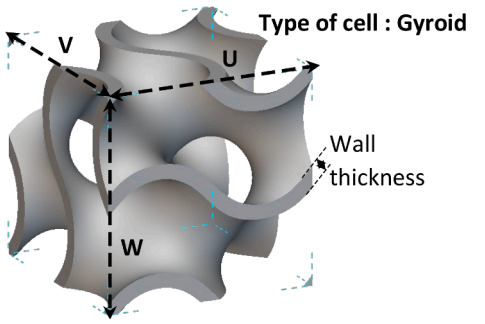

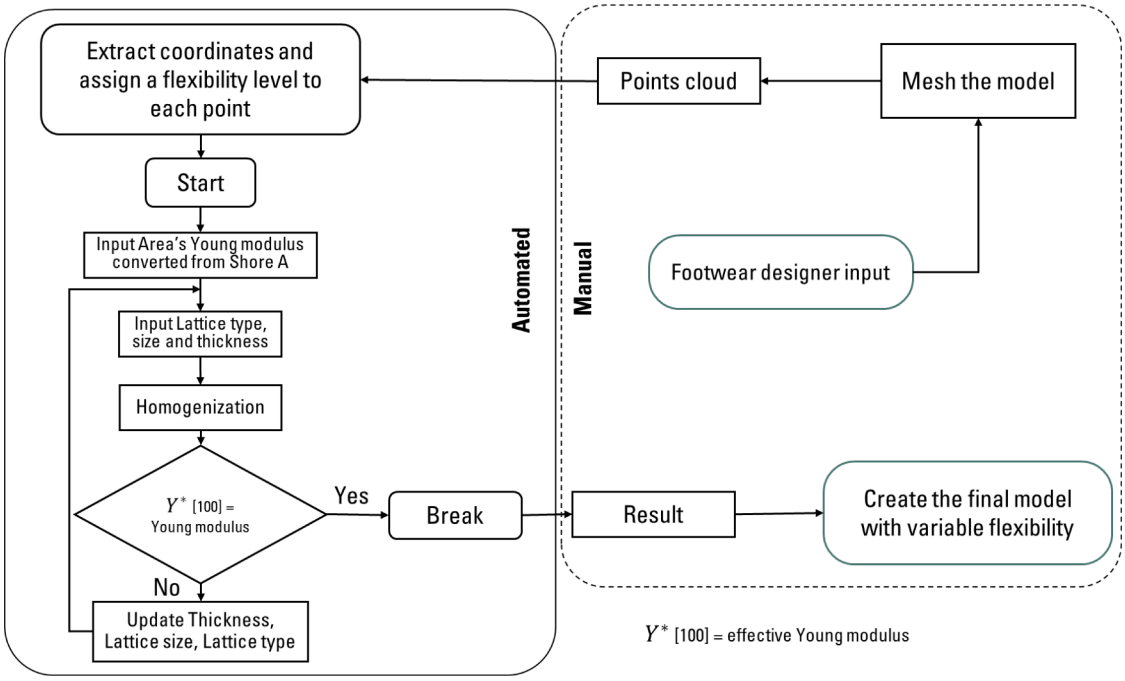

Fig. 8. Algorithm for optimizing the unit cell parameters to achieve the targeted flexibility at any point.

Table 4
Average uniaxial tensile tests results.

Material	Mean UTS [MPa] (SD)	CoV [%]	Mean E [%] (SD)	CoV [%]	Mean Y [MPa] (SD)	CoV [%]
EOS PA2200 As printed	52.0 (0.42)	0.80	18.8 (2.60)	13.79	2135.8 (142.64)	6.68
EOS PA2200 Vapor Polished	54.1 (0.71)	1.31	18.9 (2.04)	10.77	2093.0 (48.94)	2.34

UTS = Ultimate Tensile Strength; E = Elongation at break; Y = Young Modulus; (SD) = standard deviation; CoV = Coefficient of Variance.

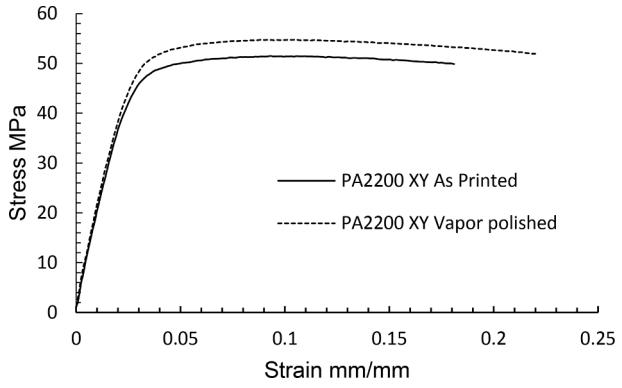

Fig. 9. Difference in stress–strain behaviour between the as-printed and vapor polished SLS fabricated PA2200 samples.

3.3.2. *Weight distribution*

The calculation of the weight distribution is based on the experimental work of Shang et al [74], which was carried out on twenty adult female volunteers with a weight of (53.56 ± 5.75 kg) and an age of (20.89 ± 3.04 years) and which consists of measuring (using an F-Scan® measuring device from the manufacturer Tekscan® [75]) the distribution of forces applied to different types of footwear during their use. A static study was carried out by simulating the application of pressure on the different plantar zones described above according to Table 5.

For simplification and reduction of computational time, the upper part was cut at the height of the outer sole and a FEA was performed, simulating the application of pressure on the different plantar zones described above, which is discussed in the previous section.

3.3.3. *Snapfit integration performance*

The FEA simulation was performed on the NASTRAN solver version 17.0.0.21 [73] through the Fusion 360 software [50]. A quadratic tetrahedral mesh size based on the 1% model and an adaptive mesh size refinement based on the accuracy of the Von Mises constraint with a convergence rate tolerance of 5% were configured. Since the objective of this part of the study is to analyze the behavior of the shoe under gait loading, a bonded type of contact was implemented between the upper part and Outsole surfaces. This setting results in a total of 370,897 mesh elements for the two parts with the worst aspect ratio of 9 out of 4% of the elements located at non-critical locations of the analyzed parts. Fig. 12 illustrates the convergence rate for 9 iterations of adaptive refinement, a convergence rate close to 1% is recorded for the total displacement, validating the satisfying quality of the FEA simulation.

Fig. 13 illustrates the results of the FEA of the shoe loading with the weight distribution described above. Fig. 13-a presents the mapping of the resulting displacement (mm) on the upper part; the maximum displacement is less than 1 mm and is located at the rear end of the shoe (MH and ML). Fig. 13-b represents the resulting displacement (mm) on the Nylon 12 (PA12) printed Outsole and indicates that the maximum displacement is 0.43 mm under 6.09 kPa and is located at the Midfoot (MF). The bending at the MF can be limited by integrating a metal part (shank) to prevent material fatigue due to repeated loading on it. The integration of the snapfit does not create a weak zone, despite the hollow space provided for its assembly, due to the steel pin A36 inside the high heel, which plays a central role in the absorption of loads applied to the shoe. It should be noted that all the calculations presented in the results section have been carried out with the characteristics of materials not treated on the surface (i.e. non Vapor Polished).

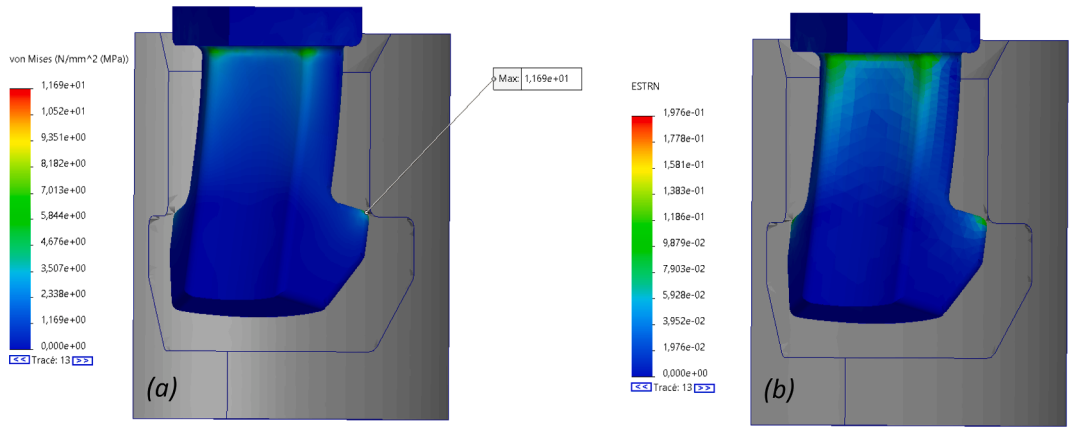

Fig. 10. Distribution of **(a)** Von Mises stress and **(b)** equivalent strain in the designed snapfit model.

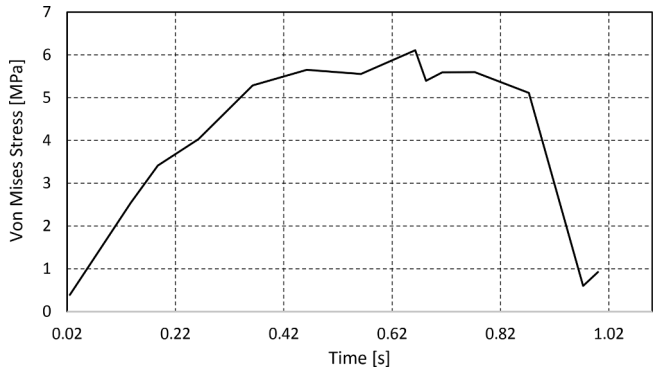

Fig. 11. Nonlinear Von Mises stress in function of time at the base of each leg.

3.4. Topology optimisation and weight reduction

A topological optimization was performed having as objective function a minimum difference between the calculated effective Young's modulus (Y*) and the Y converted from Shore A hardness data shown in Fig. 7 for each shoe area. Using the Block "Homogenize Unit Cell", the nTop platform allows us to obtain the elasticity tensor for each cell configured as mentioned above, we must therefore calculate Y* in all directions as well as the shear modulus and the Poisson ration, and for that we use the characteristic parameters of the fourth order elasticity tensor [76,77]. We will use a modified and adapted version of MATLAB program published by Nordmann et al. [76] to perform the calculations and the spatial representation of Y* as well as the shear modulus and the Poisson ratio [76].

The results of the optimization lead to the selection of the Diamond type unit cell for its large spread of values of the Y* as a function of the geometrical parameters, which provides more possibilities to vary the flexibility of the architected material.

Fig. 14 shows the linear evolution of the Y* as a function of wall thickness for different sizes of Diamond unit cells after homogenization. The effective Young's modulus (Y*) evolves positively with increasing wall thickness and decreases with increasing nominal unit cell size *a*. The filled markers in Fig. 14 denote the cell parameters chosen for the different regions to obtain the targeted effective Young's modulus. Having an interval for each region *n* of the shoe (see Fig. 7), a rule has been applied to select the points closest to the mid-ranges of Y given in Table 2, as expressed by equation (14):

$$Y^*(n) = \min\left(Y^* - \left(\frac{Y_2 + Y_1}{2}\right)\right) \tag{14}$$

Table 5
Distribution of pressure on the assembled shoe based on [74].

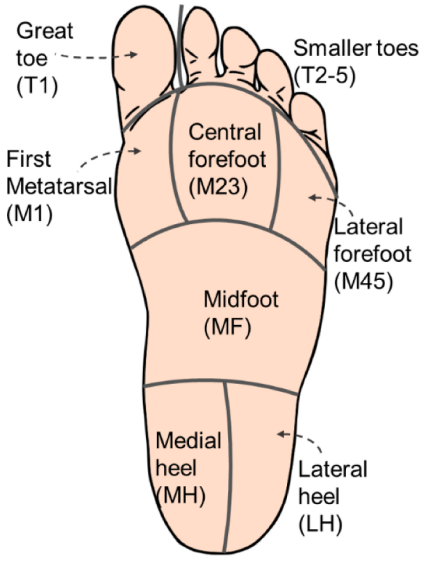

Contact Area	Surface [mm^2]	Pressure [kPa]
T1	537	13,79
T2-5	796	10,6
M1	721	17,27
M23	662	18,09
M45	639	9,59
MF	626	6,09
MH	1285	10,42
ML	943	8,79

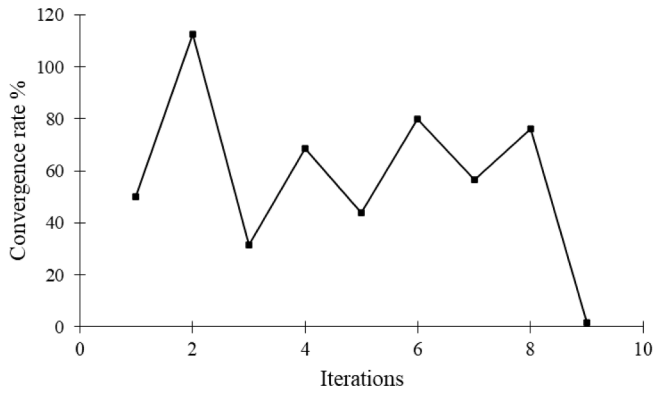

Fig. 12. Adaptative mesh size refinement: Convergence rate for each iteration.

Where Y1 and Y2 are the lower and upper limits of the Young's modulus range calculated using Mix and Giacomin's method [66]. The following values were selected for the regions n = 1, 2, 3, 4; Y*(1) = 5.16 MPa, Y*(2) = 10.71 MPa, Y*(3) = 4.58 MPa, Y*(4) = 3.48 MPa.

Fig. 15 represents the spatial (direction dependent) visualization of the calculated effective parameters such as Y*, G* and V* for each area 1 to 4 (see Fig. 7). In this case study, the architected material's elastic characteristics can be manipulated to control the flexibility by reorienting the unit cell, although this feature will not be utilized. Instead, all cells will be oriented such that the maximum Y*max aligns with the direction normal to the upper part of the shoe at all points. Since it is assumed that the material is cubic elastic, the Zener ratio [78] is also calculated to evaluate the degree of elastic anisotropy of the created structures. $Z = 2C_{44}/(C_{11} - C_{22})$ where $C_{11}, C_{22} and, C_{44}$ are component of the stiffness tensor presented in equation (11). A Zener ratio of 1 represents an isotopically elastic structure and the larger the deviation the more anisotropic the cellular material.

A variable flexibility has been implemented for the high-heel shoe to ensure the required user comfort (flexibility/stiffness), following footwear industry recommendations (see Fig. 7), with a monolithic (upper) part as shown. Fig. 16 presents this stiffness variation, which was realized by the unit cell variation in the targeted zones, including a transition gradient between each zone to ensure proper fabrication by AM and avoiding stress concentrators. A significant mass reduction of this essential high-heel component (upper part) was realized, i.e. the mass was reduced from 55.6 g for the original part to 36.5 g for the new design with the lattice structure. Hence, a 34% mass reduction is achieved, which contributes to the main objective of the present study aiming to minimize the use of raw materials towards a more sustainable and circular manufacturing approach for the footwear industry.

4. Conclusion

In summary, this study has successfully demonstrated the development of a comprehensive approach for footwear manufacturing focused on design for disassembly using AM techniques, enabling the realization of a fully 3D printed footwear product for the first time. By taking advantage of the benefits of AM as fabrication method, including new design possibilities and glueless assembly by snapfit systems, the proposed approach reduces the number of parts used for footwear production and improves the re-manufacturability and recyclability of (high-heeled) shoes. The footwear design was validated by finite element analysis, based on the use of PA2200 and TPU polymeric materials as AM feedstock, and an assembly and disassembly system compliant with industrial standards, such as SATRA TM113:1996, was developed. Indeed, it was demonstrated that the snapfit disassembly force equals 63.63 kgf, which exceeds the minimum 40 kgf recommended by the footwear industrial SATRA standard. As well, the selected polymer material was tested on mechanical performance (tensile strength) with and without a vapor polishing treatment after AM

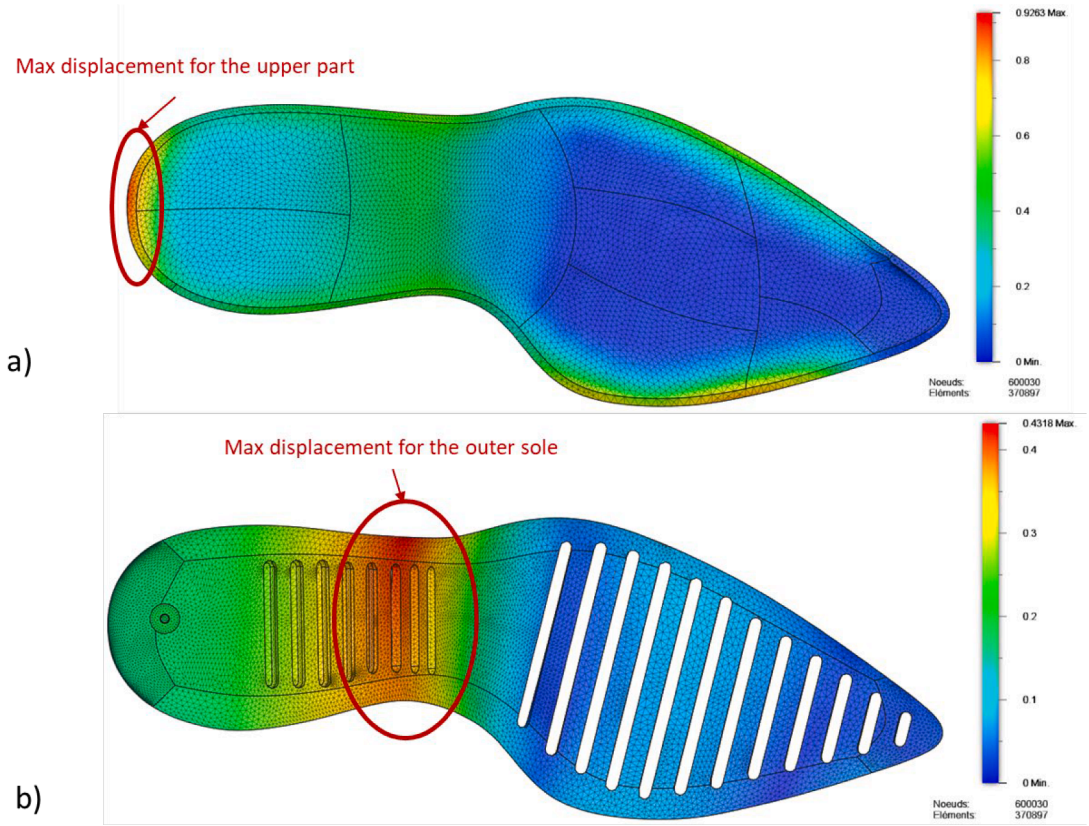

Fig. 13. Total displacement mapping in millimeter (mm) of the developed shoe components, presenting **(a)** the bottom part of upper part, and **(b)** the outer sole.

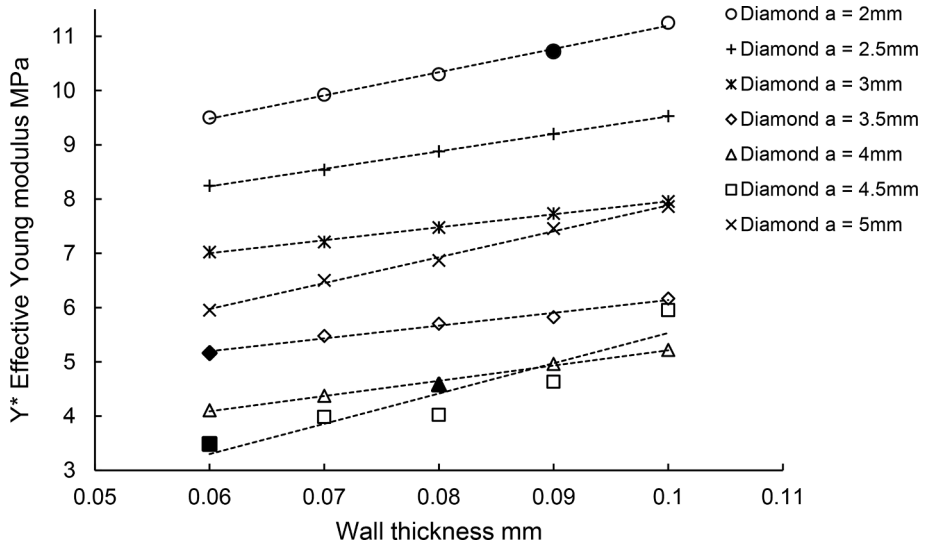

Fig. 14. Evolution of effective Young's moduli as a function of wall thickness for the Dimond cell and different cell sizes. The highlighted points represent the parameters chosen for the different shoe areas.

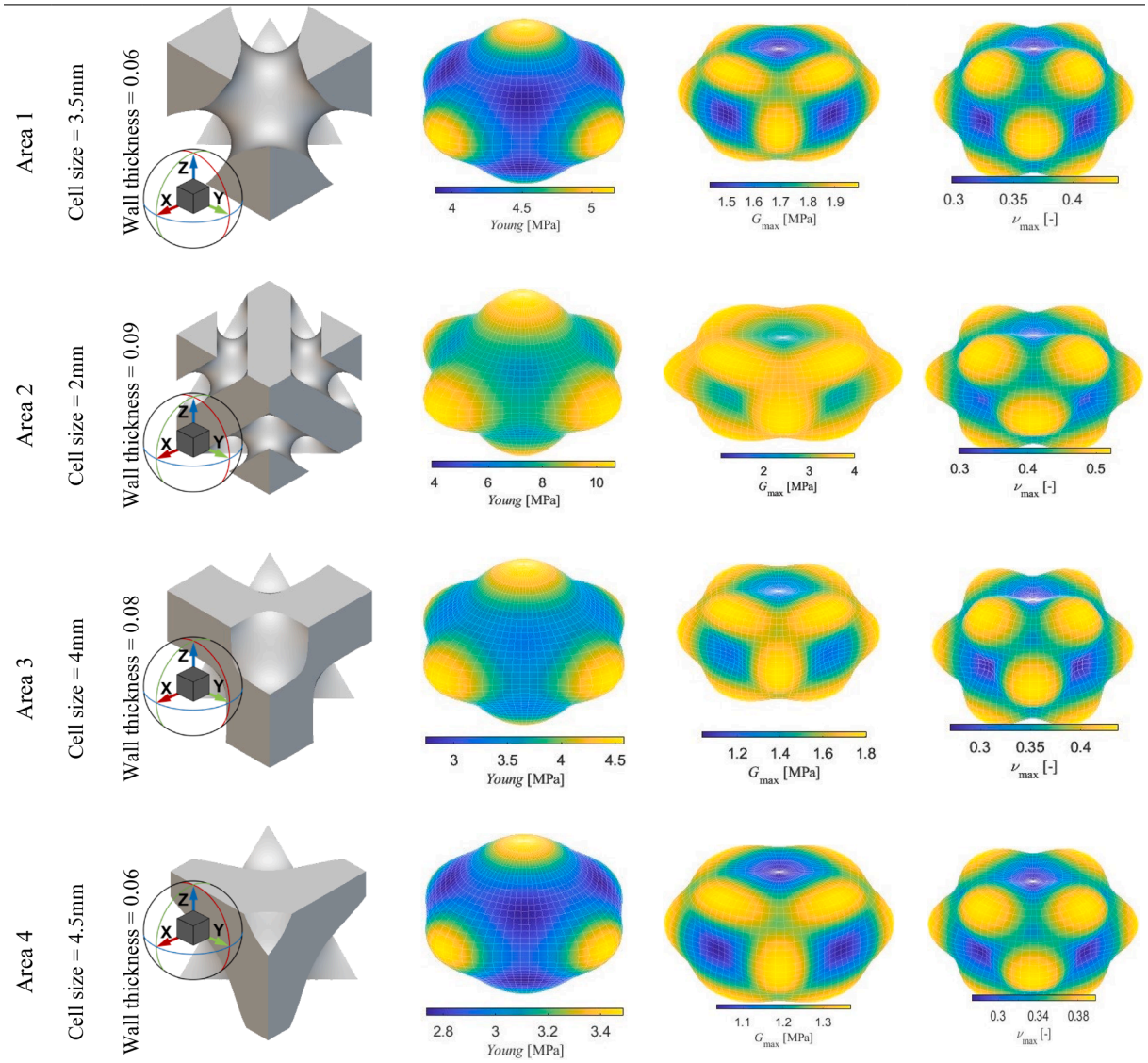

Fig. 15. Spatial visualisation of effective Young's moduli (Y*), Shear moduli (G*) and Poisson Ratio (V*) for the selected unit cells.

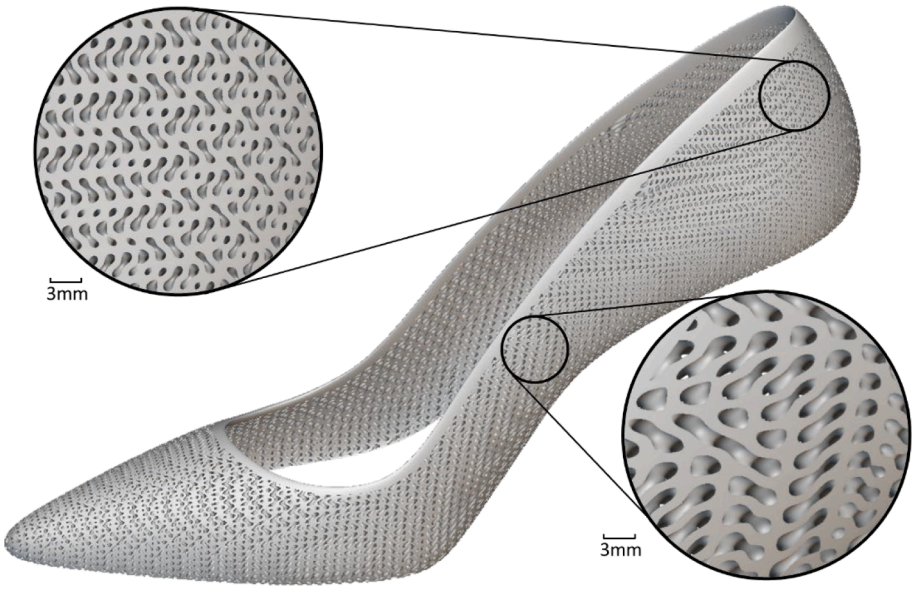

Fig. 16. Applied lattice structure on the developed high-heel shoe according to the optimisation results.

sample fabrication.

In addition, a topological optimization algorithm was implemented to reduce the mass of the shoe by 34% while achieving variable flexibility in a monolithic product, following footwear industrial standards for required comfort and durability. Overall, the developed approach is consistent with the footwear industry's goal of reducing the environmental impact and increasing the durability of its products. Future work includes physical testing of the designed parts and the multi-material snapfit system to further validate their mechanical characteristics (e.g. on elasticity and on wear and tear) and performance for consumer's usage.

Declaration of Competing Interest

The authors declare that they have no known competing financial interests or personal relationships that could have appeared to influence the work reported in this paper.

Data availability

The raw and processed data, including developed codes for the topology optimization, required to reproduce the findings reported in the present study are available to download from https://github.com/ChahGhim/Topo-Optimisation_Footwear.

Acknowledgements

The authors would like to acknowledge the financial support of the Natural Sciences and Engineering Research Council of Canada (NSERC) under the Discovery Grant (RGPIN-2018-05292 and RGPIN-2019-05973) as well as the financial support of the Mathematics of Information Technology and Complex Systems (Mitacs) Accelerate Grant IT IT28262 and ARSHAE, Montréal, Canada. Furthermore, the authors would like to thank ARSHAE's expert team for the fruitful discussions on footwear design.

References

[1] WWF, "Biodiversity, biocapacity and better choices," in "Living Planet Report," ISBN 978-2-940443-37-6 2012. [Online]. Available: http://awsassets.panda.org/downloads/1_lpr_2012_online_full_size_single_pages_final_120516.pdf.
[2] Overshoot. "Past Earth Overshoot Days." Earth Overshoot Day. https://www.overshootday.org/newsroom/past-earth-overshoot-days/ (accessed 07-01-2022).
[3] OCDE, Material Resources, Productivity and the Environment. 2015.
[4] R. Bleischwitz, P. Welfens, and Z. Zhang, "Sustainable Growth and Resource Productivity Economic and Global Policy Issues (ed. Bleischwitz," 01/01 2009.
[5] CLIMATEWATCH. "Dataexplorer." https://www.climatewatchdata.org/data-explorer/historical-emissions?historical-emissions-data-sources=cait&historical-emissions-gases=all-ghg&historical-emissions-regions=All%20Selected&historical-emissions-sectors=total-including-lucf%2Ctotal-including-lucf&page=1#data (accessed 13-07-2022, 2022).
[6] J. Eder-Hansen *et al.*, "Pulse Of The Fashion Industry 2017," 2017.
[7] M.J. Lee, S. Rahimifard, An air-based automated material recycling system for postconsumer footwear products, Resour. Conserv. Recycl. 69 (2012) 90–99, https://doi.org/10.1016/j.resconrec.2012.09.008.
[8] Ellen MacArthur Foundation, "Towards a circular economy: business rationale for an accelerated transition," 2015.
[9] F. Mathieux, et al., Critical raw materials and the circular economy, Publications Office of the European Union, Bruxelles, Belgium, 2017.
[10] W.R. Stahel, History of the Circular Economy. The Historic Development of Circularity and the Circular Economy, in: S. Eisenriegler (Ed.), the Circular Economy in the EuropeAn Union: An Interim Review, Springer International Publishing, Cham, 2020, pp. 7–19.
[11] W. McDowall, Y. Geng, B. Huang, E. Barteková, R. Bleischwitz, S. Türkeli, R. Kemp, T. Doménech, Circular Economy Policies in China and Europe, J. Ind. Ecol. 21 (3) (2017) 651–661.
[12] I.S. Jawahir, R. Bradley, Technological Elements of Circular Economy and the Principles of 6R-Based Closed-loop Material Flow in Sustainable Manufacturing, Procedia CIRP 40 (2016) 103–108, https://doi.org/10.1016/j.procir.2016.01.067.
[13] V. Delpla, J.-P. Kenné, L.A. Hof, Circular manufacturing 4.0: towards internet of things embedded closed-loop supply chains, Int. J. Adv. Manuf. Technol. 118 (9) (2022) 3241–3264, https://doi.org/10.1007/s00170-021-08058-3.
[14] Ellen MacArthur Foundation and IDEO. "The Circular Design Guide." https://www.circulardesignguide.com/methods (accessed 13-07-2022, 2022).
[15] Ellen MacArthur Foundation. "Circular Design." https://archive.ellenmacarthurfoundation.org/explore/circular-design (accessed 13-07-2022, 2022).
[16] G. Boothroyd, "Product design for manufacture and assembly," *Computer-Aided Design,* vol. 26, no. 7, pp. 505-520, 1994/07/01/ 1994, 10.1016/0010-4485(94)90082-5.
[17] A. Su, S.J. Al'Aref, Chapter 1 - History of 3D Printing, in: S.J. Al'Aref, B. Mosadegh, S. Dunham, J.K. Min (Eds.), 3D Printing Applications in Cardiovascular Medicine, Academic Press, Boston, 2018, pp. 1–10.
[18] H. Hegab, N. Khanna, N. Monib, A. Salem, Design for sustainable additive manufacturing: A review, Sustain. Mater. Technol. 35 (2023) e00576.
[19] M. Sauerwein, E. Doubrovski, R. Balkenende, C. Bakker, Exploring the potential of additive manufacturing for product design in a circular economy, J. Clean. Prod. 226 (2019) 1138–1149, https://doi.org/10.1016/j.jclepro.2019.04.108.
[20] M. Sauerwein, C. Bakker, and A. Balkenende, "Additive manufacturing for circular product design : A literature review from a design perspective," in *PLATE: Product Lifetimes And The Environment: Conference Proceedings of PLATE 2017,* , Delft, Netherlands, 8-10 November 2017 2017, vol. 9: IOS Press, p. 358, 10.3233/978-1-61499-820-4-358.
[21] WorldFootwear.com, "Word Footwear Yearbook 2020," 2020. Accessed: 05-03-2023. [Online]. Available: file:///C:/Users/15146/Downloads/wf20201557987749.pdf.

[22] L. Cheah, N.D. Ciceri, E. Olivetti, S. Matsumura, D. Forterre, R. Roth, R. Kirchain, Manufacturing-focused emissions reductions in footwear production, J. Clean. Prod. 44 (2013) 18–29.
[23] C. F. S. Commitment, "Final Report," Global Fashion Agenda 2020.
[24] D. Beiderbeck, H. Krüger, T. Minshall, The future of additive manufacturing in sports, in: In *21st century sports*: SprInger, 2020, pp. 111–132.
[25] V. Manoharan, S.M. Chou, S. Forrester, G.B. Chai, P.W. Kong, Application of additive manufacturing techniques in sports footwear: This paper suggests a five-point scoring technique to evaluate the performance of four AM techniques, namely, stereolithography (SLA), PolyJet (PJ), selective laser sintering (SLS) and three-dimensional printing (3DP), in four important aspects of accuracy, surface finish, range of materials supported and building time for prototyping sports footwear, Virtual Phys. Prototyping 8 (4) (2013) 249–252.
[26] T. Spahiu, H. Almeida, A. Manavis, P. Kyratsis, A. Jimeno-Morenilla, in: Proceedings of the 1st International Conference on Water Energy Food and Sustainability (ICoWEFS 2021), Springer International Publishing, Cham, 2021, pp. 699–707.
[27] M. Kreutz, A. Böttjer, M. Trapp, M. Lütjen, M. Freitag, Towards individualized shoes: Deep learning-based fault detection for 3D printed footwear, Procedia CIRP 107 (2022) 196–201, https://doi.org/10.1016/j.procir.2022.04.033.
[28] A. Pugalendhi, R. Ranganathan, M. Chandrasekaran, Effect of process parameters on mechanical properties of VeroBlue material and their optimal selection in PolyJet technology, Int. J. Adv. Manuf. Technol. 108 (4) (2020) 1049–1059, https://doi.org/10.1007/s00170-019-04782-z.
[29] S. Rouf, A. Raina, M. Irfan Ul Haq, N. Naveed, S. Jeganmohan, A. Farzana Kichloo, 3D printed parts and mechanical properties: Influencing parameters, sustainability aspects, global market scenario, challenges and applications, Adv. Indust. Eng. Polym. Res. 5 (3) (2022) 143–158.
[30] T. A. Osswald, "Understanding Polymer Processing," in *Understanding Polymer Processing (Second Edition)*, T. A. Osswald Ed.: Hanser, 2017, pp. I-XVI.
[31] R. Lezama-Nicolás, M. Rodríguez-Salvador, R. Río-Belver, I. Bildosola, A bibliometric method for assessing technological maturity: the case of additive manufacturing, Scientometrics 117 (3) (2018) 1425–1452, https://doi.org/10.1007/s11192-018-2941-1.
[32] *Additive manufacturing - General principles - Fundamentals and vocabulary (ISO/ASTM 52900:2021)*, ISO/ASTM, 27-04-2022 2022.
[33] L.J. Tan, W. Zhu, K. Zhou, Recent Progress on Polymer Materials for Additive Manufacturing, Adv. Funct. Mater. 30 (43) (2020) 2003062, https://doi.org/10.1002/adfm.202003062.
[34] Y. Wu, Y. Lu, M. Zhao, S. Bosiakov, and L. Li, "A Critical Review of Additive Manufacturing Techniques and Associated Biomaterials Used in Bone Tissue Engineering," (in eng), *Polymers (Basel)*, vol. 14, no. 10, May 23 2022, 10.3390/polym14102117.
[35] J. Schmidt, M.A. Dechet, J.S. Gómez Bonilla, N. Hesse, A. Bück, W. Peukert, Characterization of Polymer Powders for Selective Laser Sintering. presented at the 30th Annual International Solid Freeform Fabrication Symposium Austin, 2019.
[36] I. Gibson, D. Rosen, B. Stucker, Additive Manufacturing Technologies: 3D Printing, Rapid Prototyping, and Direct Digital Manufacturing, Springer, New York, 2014.
[37] M. Attaran, The rise of 3-D printing: The advantages of additive manufacturing over traditional manufacturing, Bus. Horiz. 60 (5) (2017) 677–688, https://doi.org/10.1016/j.bushor.2017.05.011.
[38] D. Giurco, A. Littleboy, T. Boyle, J. Fyfe, S. White, Circular economy: questions for responsible minerals, additive manufacturing and recycling of metals, Resources 3 (2) (2014) 432–453.
[39] P. Santander, F.A.C. Sanchez, H. Boudaoud, M. Camargo, Closed loop supply chain network for local and distributed plastic recycling for 3D printing: a MILP-based optimization approach, Resour. Conserv. Recycl. 154 (2020), 104531.
[40] M. Salmi, "Additive Manufacturing Processes in Medical Applications," *Materials*, vol. 14, no. 1, p. 191, 2021. [Online]. Available: https://www.mdpi.com/1996-1944/14/1/191.
[41] S.H. Khajavi, J. Partanen, J. Holmström, Additive manufacturing in the spare parts supply chain, Comput. Ind. 65 (1) (2014) 50–63, https://doi.org/10.1016/j.compind.2013.07.008.
[42] S.C. Ligon, R. Liska, J. Stampfl, M. Gurr, R. Mülhaupt, Polymers for 3D Printing and Customized Additive Manufacturing, Chem. Rev. 117 (15) (2017) 10212–10290, https://doi.org/10.1021/acs.chemrev.7b00074.
[43] N. N. Kumbhar and A. V. Mulay, "Post Processing Methods used to Improve Surface Finish of Products which are Manufactured by Additive Manufacturing Technologies: A Review," *Journal of The Institution of Engineers (India): Series C*, vol. 99, no. 4, pp. 481-487, 2018/08/01 2018, 10.1007/s40032-016-0340-z.
[44] T. Maconachie, et al., SLM lattice structures: Properties, performance, applications and challenges, Mater. Des. 183 (2019), 108137, https://doi.org/10.1016/j.matdes.2019.108137.
[45] M. Helou, S. Kara, Design, analysis and manufacturing of lattice structures: an overview, Int. J. Comput. Integr. Manuf. 31 (3) (2018) 243–261.
[46] O. Al-Ketan, R. Rowshan, and R. K. Abu Al-Rub, "Topology-mechanical property relationship of 3D printed strut, skeletal, and sheet based periodic metallic cellular materials," *Additive Manufacturing*, vol. 19, pp. 167-183, 2018/01/01/ 2018, 10.1016/j.addma.2017.12.006.
[47] S.N. Khaderi, V.S. Deshpande, N.A. Fleck, The stiffness and strength of the gyroid lattice, Int. J. Solids Struct. 51 (23) (2014) 3866–3877, https://doi.org/10.1016/j.ijsolstr.2014.06.024.
[48] V.S. Deshpande, M.F. Ashby, N.A. Fleck, Foam topology: bending versus stretching dominated architectures, Acta Mater. 49 (6) (2001) 1035–1040, https://doi.org/10.1016/S1359-6454(00)00379-7.
[49] M. Kumke, H. Watschke, T. Vietor, A new methodological framework for design for additive manufacturing, Virtual Phys. Prototyping 11 (1) (2016) 3–19, https://doi.org/10.1080/17452759.2016.1139377.
[50] *Fusion 360*. Accessed: 2023-03-23. [Online]. Available: https://www.autodesk.ca/en/products/fusion-360/features.
[51] *CATIA V5*. Accessed: 2023-03-28. [Online]. Available: https://www.3ds.com/products-services/catia/.
[52] G. Boothroyd, L. Alting, Design for Assembly and Disassembly, CIRP Ann. 41 (2) (1992) 625–636, https://doi.org/10.1016/S0007-8506(07)63249-1.
[53] nTopology_Inc. "nTop." https://ntopology.com/ (accessed 21/09/2022).
[54] EOS. "PA 2200 - Polyamide 12 White." https://www.eos.info/en/additive-manufacturing/3d-printing-plastic/sls-polymer-materials/polyamide-pa-12-alumide (accessed 09/09/2022).
[55] LehVossGroup. "LUVOSINT TPU X92A-1 NT." https://luv-lumas-online-app.azurewebsites.net/api/v1/lumas/gettdsfile/41447859/en/ISO (accessed 09/09/2022).
[56] Standard Test Method for Tensile Properties of Plastics D638, ASTM, 2014.
[57] AMTechnologies. "WHITEPAPERS & CASE STUDIES." https://amtechnologies.com/resources/ (accessed 15-09-2022).
[58] P. R. Bonenberger, "The First Snap-Fit Handbook," in *The First Snap-Fit Handbook (Third Edition)*, P. R. Bonenberger Ed.: Hanser, 2016, pp. I-XXII.
[59] Ticona, "Design calculations for snap fit joints in plastic parts," in "Calculation. Design. Application. B.3.1," 2009.
[60] J. Guo, J. Bai, K. Liu, J. Wei, Surface quality improvement of selective laser sintered polyamide 12 by precision grinding and magnetic field-assisted finishing, Mater. Des. 138 (2018) 39–45, https://doi.org/10.1016/j.matdes.2017.10.048.
[61] E. Thomasson and A. Michalska. "Adidas to mass-produce 3D-printed shoe with Silicon Valley start-up." https://www.reuters.com/article/us-adidas-manufacturing-idUSKBN1790F6?feedType=RSS&feedName=technologyNews&utm_source=Twitter&utm_medium=Social&utm_campaign=Feed%3A+reuters%2FtechnologyNews+%28Reuters+Technology+News%29 (accessed 12-09-2022).
[62] R. Teixeira *et al.*, "Towards Customized Footwear with Improved Comfort," *Materials*, vol. 14, no. 7, p. 1738, 2021. [Online]. Available: https://www.mdpi.com/1996-1944/14/7/1738.
[63] Z. Wang, A. Srinivasa, J.N. Reddy, A. Dubrowski, Topology Optimization of Lightweight Structures With Application to Bone Scaffolds and 3D Printed Shoes for Diabetics, J. Appl. Mech. 89 (4) (2022) pp, https://doi.org/10.1115/1.4053396.
[64] I.M. Methtananda, S. Parker, M.P. Patel, M. Braden, The relationship between Shore hardness of elastomeric dental materials and Young's modulus, Dent. Mater. 25 (8) (2009) 956–959, https://doi.org/10.1016/j.dental.2009.02.001.
[65] K. Larson, "Can You Estimate Modulus From Durometer Hardness for Silicones? Yes, but only roughly … and you must choose your modulus carefully!," 09/01 2017.
[66] A.W. Mix, A.J. Giacomin, Standardized Polymer Durometry, J. Test. Eval. 39 (4) (2011) 696–705, https://doi.org/10.1520/JTE103205.
[67] *Standard Test Method for Rubber Property—Durometer Hardness ASTM D2240-15 (2021)*, ASTM-International, 15 June 2021 2021. [Online]. Available: https://compass.astm.org/document/?contentCode=ASTM%7CD2240-15R21%7Cen-US&proxycl=https%3A%2F%2Fsecure.astm.org&fromLogin=true.
[68] George. Papanicolau, Alain. Bensoussan, and J.-L. Lions, *Asymptotic Analysis for Periodic Structures* (Studies in Mathematics and its Applications). 1978, p. 699.
[69] N. Strömberg, A new multi-scale topology optimization framework for optimal combinations of macro-layouts and local gradings of TPMS-based lattice structures, Mech. Based Des. Struct. Mach. (2022) 1–18, https://doi.org/10.1080/15397734.2022.2107538.
[70] K.A. Khan, F. Al Hajeri, M.A. Khan, Micromechanical modeling approach with simplified boundary conditions to compute electromechanical properties of architected piezoelectric composites, Smart Mater. Struct. 30 (3) (2021), 035013, https://doi.org/10.1088/1361-665x/abdc05.
[71] K.A. Khan, R.K.A. Al-Rub, Modeling Time and Frequency Domain Viscoelastic Behavior of Architectured Foams, J. Eng. Mech. 144 (6) (2018) 04018029, https://doi.org/10.1061/(ASCE)EM.1943-7889.0001448.
[72] M. Faes, Y. Wang, P. Lava, and D. Moens, "Variability in the mechanical properties of laser sintered PA-12 components," *Proceedings of the 26th annual international solid freeform fabrication symposium. Solid freeform fabrication symposium*, pp. 847-856, 2015.
[73] *NASTRAN*. Accessed: 2023-03-23. [Online]. Available: https://help.autodesk.com/view/NSTRN/2017/ENU/?guid=GUID-B7044BA7-3C26-49DA-9EE7-DA7505FD4B2C.
[74] J. Shang, L.i. Chen, S. Zhang, C. Zhang, J. Huang, X.u. Wang, A. Yan, X. Ma, Influence of high-heeled shoe parameters on biomechanical performance of young female adults during stair ascent motion, Gait Posture 81 (2020) 159–165.
[75] Teskan. "Teskan F-Scan System." https://www.tekscan.com/products-solutions/systems/f-scan-system (accessed 01-02-2021).
[76] J. Nordmann, M. Aßmus, H. Altenbach, Visualising elastic anisotropy: theoretical background and computational implementation, Contin. Mech. Thermodyn. 30 (4) (2018) 689–708, https://doi.org/10.1007/s00161-018-0635-9.
[77] T. Bohlke, C. Bruggemann, Graphical Representation of the Generalized Hooke's Law, Tech. Mech. 21 (2) (2001) 145–158.
[78] Z. Li, R.C. Bradt, The single-crystal elastic constants of cubic (3C) SiC to 1000° C, J. Mater. Sci. 22 (7) (1987) 2557–2559, https://doi.org/10.1007/BF01082145.